Sea ice formation, glacial melt and the solubility pump boundary conditions in the Ross Sea.

Brice Loose[1], Sharon Stammerjohn[2], Peter Sedwick[3], and Stephen Ackley[4]

[1]Graduate School of Oceanography, University of Rhode Island, Narragansett, Rhode Island 02882, USA.

[2]Institute of Arctic and Alpine Research, University of Colorado, Boulder, Colorado 80309, USA

[3]Department of Ocean and Earth Sciences, Old Dominion University, Norfolk, Virginia 23529, USA.

[4]Ctr. for Adv. Meas. in Extreme Env., University of Texas at San Antonio, San Antonio, Texas 78249, USA

Key points:

1. Noble gas tracers can infer the rate of sea ice production in polynyas.
2. Frazil ice in polynyas appears to block air-sea gas exchange mechanisms.
3. The solubility pump is influenced by glacial ice melt and sea ice formation.

Abstract:

Dense Shelf Water in the Ross Sea is a direct precursor to Antarctic Bottom Water, which fills the deep ocean, carrying gases in what composes the southern limb of the solubility pump. Here we use late fall seawater noble gas concentrations, from two Ross Sea polynyas, to decompose the physical processes that determine the solubility properties for Dense Shelf Water (DSW). This decomposition reveals 8-10 g/kg of glacial meltwater in DSW, and sea-ice production rates of up to 21 m/yr within the Terra Nova Bay polynya. Despite winds upwards of 35 m s^{-1}, during the observations, air bubble injection had a minimal contribution to the gas solubility deficit, accounting for only 0.03 μmols/kg of argon in seawater, suggesting that the two-phase slurry of frazil ice and seawater in the surface ocean really limits air-sea exchange. Most noteworthy is the revelation that sea-ice formation and glacial melt inputs restored nearly 30% of the gas solubility deficit in DSW, or 0.4 μmols/kg in terms of argon. These measurements reveal an unexpected cryogenic component of the solubility pump and demonstrate that while sea ice may block air-sea exchange, sea ice formation and glacial melt offset this effect via addition of gases. While polynyas are a small surface area region within the Southern Ocean outcrop of the meridional overturning circulation, they represent the primary ventilation site for Antarctic Bottom Water, thus suggesting that ice processes both enhance and hinder the solubility pump.

Plain language summary

Previous scientific studies have demonstrated that the water which fills the deep sea is created in isolated regions of the surface ocean where wind, evaporation, heat loss, and sea ice formation can work in concert to make very cold salty seawater at the ocean surface, and when it sinks into the deep sea it can carry oxygen and carbon dioxide, as well as heat away from the atmosphere for nearly a millennium, suggesting the sequestration mechanism may impact earth's climate and human climate change. This study sought to reveal how different types of sea ice and glacier ice might influence the gases that are dissolved in seawater and sequestered in the ocean. We made measurements of the noble gases (helium, neon, argon, krypton, and xenon) in the Ross Sea in late fall of 2017, when the conditions are cold and windy, leading to lots of dense water production. The results reveal that sea ice interrupts the process of air-sea

exchange, which can slow down the uptake of human-generated carbon dioxide by dense water. But our results also revealed that sea ice formation and glacial ice melt can both add gas to dense water during its creation.

0.0 Introduction:

Latent heat polynyas are veritable ice factories, producing a quantity of ice cover that is far out of proportion to their surface area, as much as 10% of the Antarctic ice pack is produced within an area that is ca. 1% of the seasonal maximum in ice extent (Tamura et al. 2008). This disproportionate sea ice production rate makes these features an essential component to the ventilation of Antarctic Bottom Water (AABW) (Gordon et al. 2010; Silvano et al. 2018), which is a mixture of Circumpolar Deep Water (CDW) and the Dense Shelf Water (DSW) and originates within these polynyas. In the satellite era, there has been only one documented occurrence of a sensible heat polynya (de Lavergne et al. 2014; Cheon et al. 2015), suggesting Antarctic latent heat polynyas are the primary mechanism of DSW production and thus ventilation of the deep Southern limb of the meridional overturning circulation (MOC).

The importance of polynyas to the MOC also signifies that they play a disproportionate role in controlling the solubility of carbon dioxide and oxygen, for example, in AABW (Ohshima et al. 2016). Continental shelf processes that lead to upwelling, entrainment, and biogeochemical modifications, therefore help to set the properties for AABW and control the solubility pump (Jacobs and Giulivi 2010). The role of sea-ice cover and the size of the outcropping region in models of the MOC are considered to be a key component of the solubility pump efficiency: as the area of the outcrop region shrinks (Toggweiler et al. 2003; Nicholson et al. 2010) or becomes ice-covered (Keeling 1993; Sigman et al. 2010), it enhances the ocean-atmosphere pCO_2 differential and weakens the solubility pump (Broecker et al. 1999; Toggweiler et al. 2003). This phenomenon may also impact the ocean-atmosphere oxygen differential, which suggests a reinterpretation of the oxygen decrease during glacial periods (Cliff et al. 2021).

That insight from models suggests that deep water formation in polynyas, which are disproportionately small by surface area, is perhaps the least efficient mechanism to support a robust solubility pump. However, these studies have focused exclusively on the role of sea-ice cover in reducing or inhibiting air-sea exchange (Keeling, 1993). In this study we document the role of physical processes that take place within the polynya and over the continental shelf, and we assess how these processes contribute to setting the gas solubility properties of DSW. We argue that ice processes – sea ice formation and glacier melt – act to restore a significant portion of the solubility deficit that arises as CDW upwells and is modified into DSW. We use measurements of the five inert noble gases to constrain the impact of these physical processes, and develop a budget of dissolved argon to reveal how each process contributes to the ultimate gas solubility properties observed in DSW.

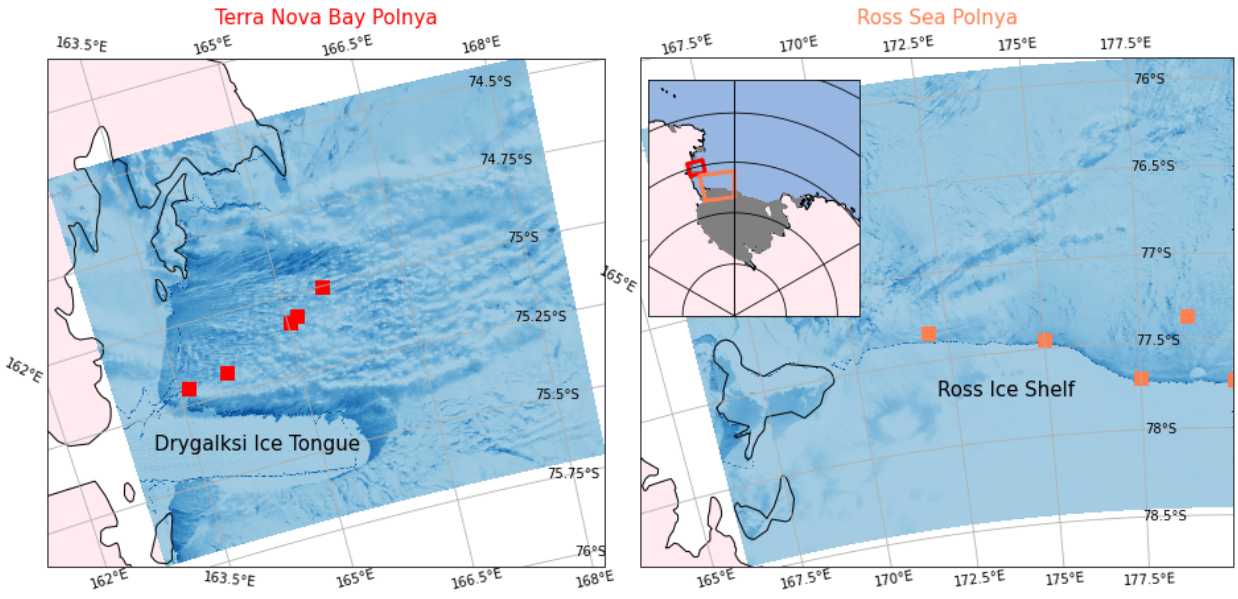

Figure 1: Map of the Terra Nova Bay (A) and Ross Sea (B) Polynyas. Square symbols indicate the hydrographic station locations. The inset in panel B reveals the location of both polynyas within the Ross Sea. MODIS visible imagery shows surface conditions at the end of March, 2017 when light was still sufficient for visible imaging.

0.1 Ross Sea Waters, the regional context and noble gas distributions:

Circumpolar Deep Water upwells latitudinally near 60 °S within the Antarctic Divergence Zone (Jenkins 2020), and the Ross Sea receives cross-shore inputs of modified CDW, which originates from the east within the Ross Gyre, and flows along the continental shelf break. This shelf-adjacent water mass is described as a 1000 m thick layer with temperature greater than 0.6 ℃ (Orsi and Wiederwohl 2009). The CDW in this region contributes significantly to the shelf break frontal system that moves intermittently onshore and offshore, releasing DSW in tidal pulses (Padman et al. 2009). These tidal currents can reach speeds of 1 m s^{-1}, particularly within the concentrated outflow regions found at the Drygalski, Joides, and Glomar Challenger Troughs in the Western Ross Sea. It further appears that these dense outflows are connected to the onshore flow of CDW. Morrison et al. (2020) used an eddy-resolving model to reveal inflows of CDW that coincide spatially and temporally with the pulsed outflow of DSW.

The Ross Sea has been experiencing a secular decrease in salinity (Jacobs et al. 2002), a process that has been associated with freshening of dense shelf water (Silvano et al., 2018), perhaps as a consequence of increased glacial melting in the Amundsen and eastern Ross Seas, which lie upstream along the Antarctic Coastal Current (Jacobs and Giulivi 2010). In Prydz Bay, East Antarctica, inputs of submarine glacial meltwater into DSW have been shown to moderate dense water production in another region (Williams et al. 2016). A recent study has documented a rebound in the salinity of DSW (Silvano et al., 2018) revealing how winds and the rate of regional sea ice production are direct drivers of DSW production on a seasonal basis, but the trend of Ross Sea freshening appears to persist over decades to the present day (Jacobs et al. 2022). Collectively, these studies reinforce what we understand to be the fundamental connection between cryogenic processes and the MOC.

The measurements used in this study were collected during austral fall, between May 1 and May 26, 2017 during the Polynyas and Ice Production in the Ross Sea (PIPERS) expedition (Ackley et al. 2020). Individual CTD profiles and water-column samples were collected in the Terra Nova Bay Polynya (TNBP) and the Ross Ice Shelf Polynya (RSP) (Figure 1). Conditions in the TNBP were significantly windier than in the RSP, with a mean wind speed of 20.3 m s^{-1} between April and October, as compared to 5.7 m s^{-1} as measured by Automated Weather Stations Manuela

(near TNBP) and Vito (near RSP). These mean wind differences reveal themselves in the water column properties (as discussed below).

The five stable noble gases - helium, neon, argon, krypton, xenon, as well as oxygen reveal the range of processes operating on dissolved gases in the actively-ventilated layers of the Ross Sea continental shelf. Some of these processes counter each other and the profiles in Fig. 2 reveal the net or accumulated effect. Helium and neon, the lightest noble gases, exhibit low solubility in seawater, but elevated concentrations in glacial ice, which traps on average 110 g of air per kg of ice (Martinierie et al. 1992). Against the background of air-sea exchange, glacial melt in the ocean produces large helium and neon excesses; up to 13% for helium in the Ross Sea (Figure 2b). Figure 2 depicts the dissolved gas saturation anomaly (Δ_i), where the gas concentration is expressed as the deviation from equilibrium saturation (Hamme and Severinghaus 2007); zero saturation anomaly reflects a water column in solubility equilibrium with the atmosphere. Panels A and B depict the conditions in the Ross Sea coastal polynyas during the PIPERS expedition, whereas panel C showcases Weddell Sea data from profiles along 57 °S, acquired further offshore in the Antarctic Circumpolar Current (ACC). These profiles from the Weddell Sea reveal the same general fractionation of noble gases based on atomic mass, but with an attenuated signal in the lighter gases, reflecting the distance from a coastal region that set the properties observed in the Ross Sea coastal polynyas.

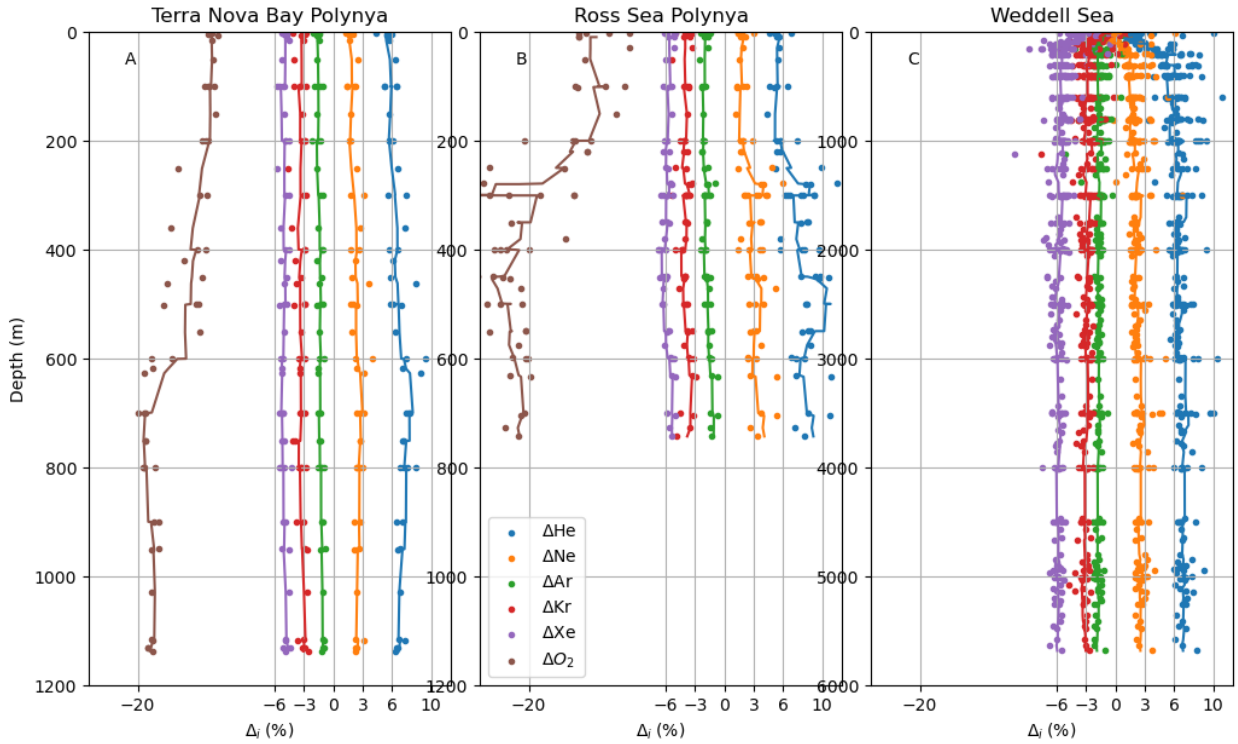

Figure 2: Saturation anomalies, $\Delta_i = (C_{obs}/C_{eq} - 1) \times 100$, where C_{obs} is the observed gas concentration and C_{eq} is the concentration in equilibrium with the atmosphere, for He, Ne, Ar, Kr, Xe and O_2.

Krypton and xenon are heavier and increasingly more soluble noble gases; their temperature-dependent solubility and slower gas exchange rates produce water column deficits during the cooling period with restricted air-sea exchange (Hamme et al. 2019). The addition of melted glacial ice can also lead to a slight deficit in Kr and Xe (Loose and Jenkins 2014), which further helps to distinguish glacial melt from air bubble injection. The deficits of Kr and Xe are most extreme in the RSP, with Xe extending below -6 %. These deficits are similar to the more offshore values in the Weddell Sea. The Terra Nova Bay polynya shows deficits that are smaller than in the Ross Ice Shelf Polynya: TNBP vertical average of -5.0 as compared to -5.8 in RSP, which is consistent with a greater quantity of glacial meltwater in the RSP.

In addition to air-sea disequilibrium and glacial meltwater, sea ice formation may alter the water column dissolved gas budgets under certain conditions (Top et al. 1988). This is caused by solute exclusion and brine rejection from the sea ice crystal lattice during freezing (Namiot and Bukhgalter 1965; Hood et al. 1998). In coastal polynyas the exceedingly high rates of sea ice

159 formation (Tamura et al. 2008; Ohshima et al. 2013) may be sufficient to influence the water
160 column noble gas excesses (Loose et al., 2016). Solute exclusion is more intensive for the heavier
161 dissolved solutes. This process can lead to greater exclusion of e.g. Kr and Xe during freezing as
162 compared to Ne and He.
163 In contrast to the inert noble gases, the profile of dissolved oxygen reflects the remnants
164 of oxygen depleted circumpolar deep waters, which are well below what can be produced from
165 physical processes alone. In the RSP, the saturation anomaly reaches Δ_{O2} = -25% at 300 m, while
166 the oxygen budget is somewhat less-depleted in the TNBP with minimum values reaching Δ_{O2} =
167 -20 %. Offshore of the continental shelf, the depletion in oxygen reaches its most extreme in the
168 core of circumpolar deep water near 400 m depth, along σ_θ = 27.77. Data from 2011 along 67 °S
169 in the CLIVAR s04p section in 2011 reveal oxygen deficits down to Δ_{O2} = -47%, which represents
170 a depletion of 155 umol/kg in O_2.
171 The noble gases can be used to reconstruct the impacts of solute inputs from sea ice
172 production, freshening from glacial meltwater, and diffusive air-sea disequilibrium at the time of
173 dense shelf water formation. We use the noble gas paleothermometer inverse model (Stute and
174 Schlosser 1993; Aeschbach-Hertig and Solomon 2013) to infer each of the contributions to shelf
175 water in the Ross Sea and Terra Nova Bay polynyas.
176
177 **1.0 Methods: The noble gas paleothermometer**

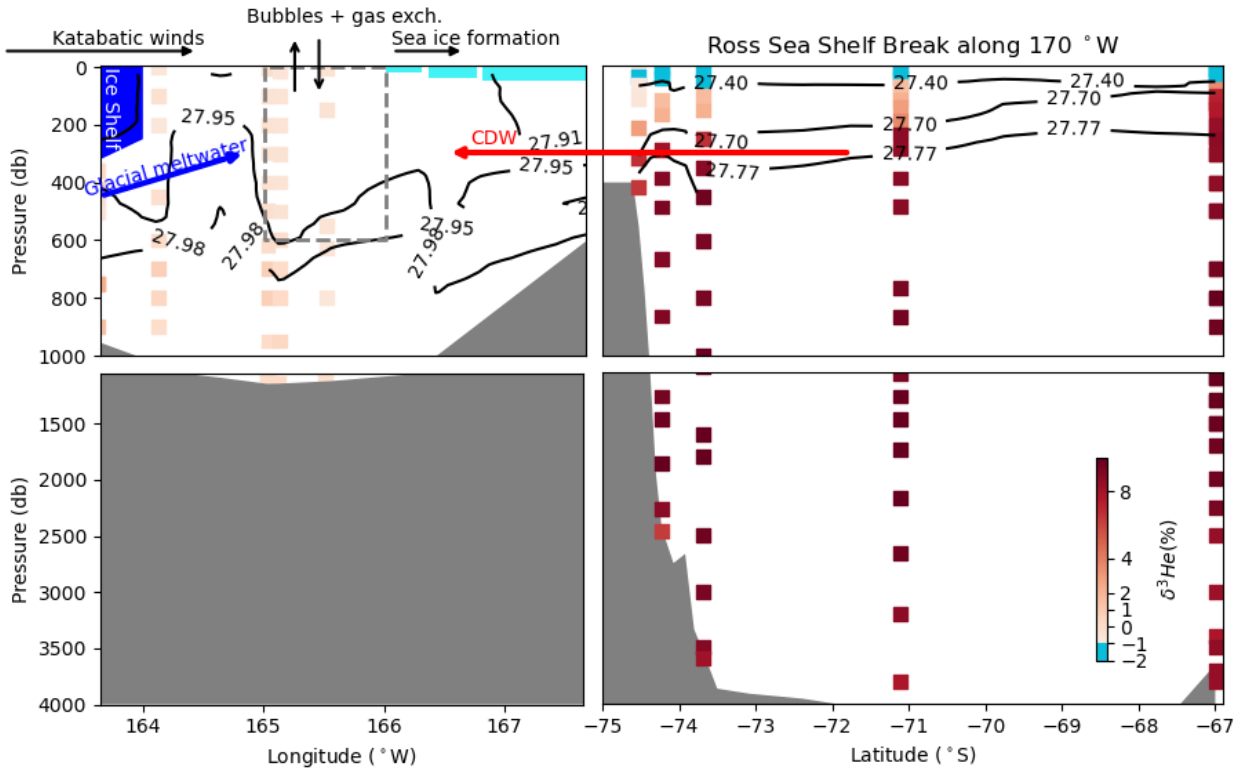

Figure 3: Profiles of δ^3He beyond the continental shelf along 170 °W, collected during the CLIVAR 2011 s04p line, and within Terra Nova Bay polynya, during the 2017 PIPERS expedition. The δ^3He traces the on-shore transport of circumpolar deep water and the ventilation process that takes place within the polynya. The schematic arrows depict the contributions of individual processes and water masses to the water column profiles in the polynya box, indicated by a dashed line.

The noble gas paleothermometer (NGPT) attempts to distinguish the physical processes that establish dissolved gas and thermohaline properties of surface water as it is modified to become interior water. The method was originally developed to quantify air entrainment during groundwater aquifer recharge (Stute and Schlosser 1993; Aeschbach-Hertig and Solomon 2013). In this study and in Loose et al., (2016) we have adapted the NGPT to infer the abundance and distribution of CDW and DSW in addition to diffusive air-sea gas exchange (driven mostly by rapid cooling of the water parcel), air bubble injection, glacial meltwater inclusion, and sea ice formation. The descriptive picture is that of a water mass being acted upon by strong winds and cold air temperatures which lead to extreme heat loss and in-situ formation of frazil ice (Figure 3). During the PIPERS expedition, frazil ice formation was extensive throughout the TNBP during

two katabatic wind events (Ackley et al. 2020; Tison et al. 2020). During the specific conditions when we observed frazil ice formation, temperature and salinity anomalies in the surface ocean were observable during repeated CTD profiles (Thompson et al. 2020).

Referring to the schematic polynya box (dashed line in Fig. 3), the NGPT begins with a mass conservation statement, which also reveals how polynya processes lead to modifications of the individual water properties. The observed inert noble gas concentrations are used to constrain a mass balance of Shelf Water (SW), Circumpolar Deep Water (CDW), Glacial Meltwater (GMW), and the water lost to sea ice production, or Sea Ice Water (SIW):

$$M_{obs} = M_{sw} - M_{siw} + M_{gmw} + M_{cdw} \quad (1)$$

Sea Ice Water refers to the mass of water that has been removed from the box through sea ice formation and advection by surface winds, and M_{siw} is explicitly defined as a loss term. We can simplify the conservation statement by first expressing the masses of each tracer as the product of the volume of seawater or sea ice (e.g. V_{gmw} is the volume of glacial meltwater), ρ is the density of water or ice, and C is the concentration in micromoles per kilogram of seawater. Note, we have made the approximation that the differences in density between the water masses are small enough to be neglected:

$$C_{obs}V_{tot}\rho_w = [\beta(S,T)\chi + A\chi]V_{sw}\rho_w - \rho_{ice}C_{ice}V_{siw} + V_{gmw}C_{gmw}\rho_w + V_{cdw}C_{cdw}\rho_w \quad (2)$$

In equation (2) we have explicitly defined tracer concentration in Shelf Water as:

$$C_{sw} = [\beta(S,T)\chi + A\chi] \quad (3)$$

The two terms on the right of equation (3) represent the atmospheric gases in SW. These are determined using the equilibrium solubility coefficient (**β**) and the molar mixing ratio of each gas in air, (χ), which is constant for each of the noble gases. The mass of each gas injected through air bubbles is the product of the molar concentration of air dissolved in water (A) with χ, the molar mixing ratio.

Sea ice formation results in the partitioning of dissolved solutes between brine pockets that are included within the ice, and dissolved solutes that are immediately or eventually deposited in the water parcel beneath sea ice (Killawee et al. 1998). This process of solute exclusion is complex and evolves through several phases that include near instantaneous segregation during formation of individual ice crystals as well as brine drainage, which happens over time as the individual brine pockets coalesce into brine channels (Wettlaufer 1992; Feltham et al. 2006). Here, the treatment of brine drainage and solute exclusion is somewhat coarse, but is an adequate approximation given what residual solutes can be measured in the water column. The near-equilibrium partitioning between the concentration of solutes in ice (C_{siw}) can be related to the concentration of the same solute found in the ambient water (C_{eq}) in our case.

$$\kappa_{iw} = \frac{C_{siw}}{C_{eq}} \tag{3}$$

The term, κ_{iw} is the ice-water partition coefficient (Garandet et al. 1994) and it has been estimated for a variety of solutes, including the noble gases and salt. Here, dissolved helium is unique from the larger noble gases, because it appears to prefer incorporation into the sea ice lattice structure, producing a value of $\kappa_{iw} > 1$. All other gases are preferentially excluded. The values of κ_{iw} are individually listed in the caption of Table 1.

Because it is not practical to make direct measurements of C_{siw} the tracer concentration in the ice, equation (3) can be used to substitute C_{siw} for C_{eq} in equation (2). This permits the expression of the mass of sea ice water removed in terms of the ambient tracer concentrations (C_{eq}): $C_{siw} = \kappa_{iw} C_{eq}$ By dividing the R.H.S. of equation (2) by V_{tot}, we obtain the water mass fractions that characterize the NGPT, e.g. $f_{gmw} = \frac{V_{gmw}}{V_{tot}}$. Gathering the terms, equation (2) simplifies to:

$$C_{obs} = [\beta(S_{sw},T)\chi + A\chi](f_{sw}) - \kappa_{iw}\beta(S_{sw},T)_{sw}\chi\frac{\rho_{ice}}{\rho_{sw}}f_{siw} + f_{gmw}C_{gmw} + f_{cdw}C_{cdw} \tag{4}$$

Equation (4) expresses the observed concentration in terms of the unknown properties of interest: f_{sw}, f_{siw}, f_{gmw}, f_{cdw}, A, and S_{sw}. Respectively, these are the water mass fractions, the moles

of air per kg of seawater, and the salinity of shelf water. The term S_{sw} is allowed to vary as a parameter in the model to reflect the likelihood that the gas is not in equilibrium with the atmosphere and will therefore lead to diffusive gas exchange (Loose et al., 2016). As with Loose et al., (2016), we use a constant pressure value of 0.97 atmospheres to reflect the persistent low pressure over the latitudes of the Ross Sea (Allan and Ansell 2006; Costanza et al. 2016), rather than admitting atmospheric pressure as a free parameter in the NGPT. During the PIPERS expedition, most of the water column in the TNBP and RSP was at or below the freezing point, so the temperature parameter space is restricted at the lower limit leading us to use the in-situ temperature and remove temperature as a free parameter from the model. Equation (4) requires a non-linear optimization technique to account for the changes in β, which are non-linearly dependent on S_{sw}. Further details on the optimization can be found in Loose et al., (2016).

In addition to equation (4), water continuity provides an additional constraint to ensure that all the water mass fractions sum to 1. Equation (4) also takes a slightly different form for heat and salt conservation. As with the other dissolved solutes, salt is excluded during the seawater freezing process: bulk sea ice salinity is typically ⅓ of the salinity found in the subnatant seawater (Thomas and Dieckmann 2010). Therefore, we employ a partition coefficient of κ_{iw} = 0.33 for salt. Salinity is not a volatile solute, so it is neither affected by air-sea gas exchange nor air bubble injection.

The argument for the heat budget is slightly different from the salt budget. Heat transfer at the air-sea interface has many pathways, including latent, sensible, and radiative heat transfer. There is no known partitioning coefficient for heat exclusion from ice. However, freezing is accompanied by a heat loss in the form of latent heat. Away from the air-sea interface, we argue that all this heat transfer takes place between the liquid and solid phase of H_2O (Gade 1979; Jenkins 1999). This is the argument used to define the glacial meltwater end member. Sea ice formation is not as straightforward, because much of the latent heat is likely lost to the atmosphere. During PIPERS, Thompson et al., (2020) observed anomalies of heat and salt directly beneath the air-water interface in the intense periods of katabatic wind activity. These anomalies were concluded to be the result of ice formation. In their budget analyses, the mass of heat and salt were not proportionate. Instead, the excess heat was about 25% of the excess salt. As stated

above, long-term observations indicate that sea ice achieves an average salinity that is approximately 33% of the seawater salinity before freezing. These suggest a 'partition coefficient' for heat that is 0.25*(1-0.33) = 16.7% of the initial heat content.

To formulate the heat budget during sea ice formation, we first imagine that no heat is lost to the atmosphere, so the heat balance is:

$$Q_{siw} = Q_{ice} + Q_{lf} \tag{5}$$

where Q_{siw} is the heat content of water tied up in sea ice and lost from the system, and Q_{lf} is the heat transferred by latent heat release. Expanding the heat balance equation using $\rho,\ c_p,\ T,\ V$ the density, specific heat capacity, temperature and volume gives:

$$\rho_w V_{siw} c_{pw} T_{siw} = \rho_{ice} V_{ice} c_{p,ice} T_{ice} + \rho_{ice} V_{ice} L_f \tag{6}$$

The heat budget for sea ice formation is next substituted into the heat conservation equation, which mirrors equation (4):

$$Q_{obs} = Q_{sw} - Q_{ice} + Q_{cdw} + Q_{gmw} \tag{7}$$

Equation (7) can be expanded using the same $\rho,\ c_p,\ T,\ V$ terms, substituting for Q_{siw} with equation (6), and dividing through by $\rho_w V_w c_{pw}$ yields:

$$T_{obs} = f_{sw} T_{sw} - f_{siw} T_{sw} + 0.167 f_{siw} \frac{L_f}{c_{p,sw}} + f_{cdw} T_{cdw} + f_{gmw} T_{gmw} \tag{8}$$

Based upon the observational results of Thompson et al., (2020) the addition of latent heat during sea ice formation is diminished by the factor of 0.167.

In summary, we can write versions of equation (4) for each of the five noble gases, as well as temperature and salinity. The conservation of water provides one additional constraint yielding a total of 8 equations on 6 free parameters.

2.0 Results and Discussion:

The properties used to define the individual water types in the NGPT model are listed in Table 1. The suitability of the NGPT solution to the data is evaluated by observing the residuals or model-data misfit. Following (Tomczak, 1981; Tomczak & Large, 1989), a misfit of less than 5% between model and data is considered an acceptable solution. The reconstruction of neon and xenon show the greatest misfit between model and data; both range between +/- 2% total misfit (Figure S1). The reconstruction of water conservation, temperature and salinity are all less than 0.1% misfit, demonstrating that the model is able to reproduce all the input constraints.

Table 1: List of properties for each of the end member values and free parameters in the NGPT model. The values for CDW were determined using offshore profiles from the Weddell and Amundsen Seas. The values for GMW were derived using the average air content of glacial ice from Martiniere (1992), and the values for SIW were determined using the equilibrium partition coefficient defined in equation (3), for He: 1.33, Ne: 0.83, Ar: 0.49, Kr: 0.4, Xe: 0.5. The N/I terms signify values that were 'not included' because the individual tracer (column) has no impact on the given process or water mass (row).

	Heat (°C)	Salt (gkg^{-1})	He (µmol kg^{-1})	Ne (µmol kg^{-1})	Ar (µmol kg^{-1})	Kr (µmol kg^{-1})	Xe (µmol kg^{-1})
SW	T_{obs}	Free param. of interest	Free param. of interest: $[\beta_i(S_{sw},T)\chi_i + A\chi_i]f_{sw}$				
CDW	1.63	34.7	0.0019	0.008	16.25	0.0039	0.0006
GMW	-92	0	0.025	0.086	44.23	0.005	0.004

SIW	$T_{obs} + 0.167 f_{siw} \frac{L_f}{c_{p,sw}}$	$0.33 S_{sw}$	Free param. of interest: $\beta_i(S_{sw}, T)\chi_i \kappa_{iw}$				
S_{sw}	N/I	Free param. of interest	N/I	N/I	N/I	N/I	N/I
Air	N/I	N/I	Free param. of interest: $A\chi_i$				

Figure 4 depicts the five outputs from the NGPT model: f_{sw}, f_{cdw}, f_{gmw}, f_{siw}, S_{sw}, and Air injection together with the in-situ temperature and salinity. Shelf Water is the predominant water property reflected in these late fall profiles; in the TNBP Shelf Water is vertically uniform near 90% of the water column by water mass composition. In the RSP, Shelf Water is ca. 85% with the exception of a broad region between 200 and 600 m, where the SW distribution decreases to a minimum of 70%. This mid-depth region in the RSP is the primary area where the intrusion of modified CDW can still be identified. CDW reaches a maximum of nearly 30% by mass at 300 m. These intrusions of CDW between 300 and 600 m coincide with the lowest oxygen saturations in the water column (Fig. 2).

The water properties revealed by the NGPT highlight the apparent differences between the two polynyas in 2017. The water column in the RSP contained a broad distribution of glacial meltwater between 300 and 600 m (Fig. 4), and the remnants of a CDW intrusion were apparent along the potential density anomaly of $\boldsymbol{\sigma_\theta}$ = 27.76 (Fig. 5). Overall the RSP was more stratified than the TNBP with density stratification reaching within 250 m from the ocean surface. The potential density contours reveal observably less buoyancy loss in the water column as compared to the Terra Nova Bay Polynya (Fig. 5); potential density anomalies at the air-se interface within the open water section of the TNBP were also heavier as $\boldsymbol{\sigma_\theta}$ =27.92 as compared with $\boldsymbol{\sigma_\theta}$ = 27.76 in the RSP. However, we did not observe mixed layers that extended to the ocean bottom in either polynya as they presumably would after a full season of DSW formation.

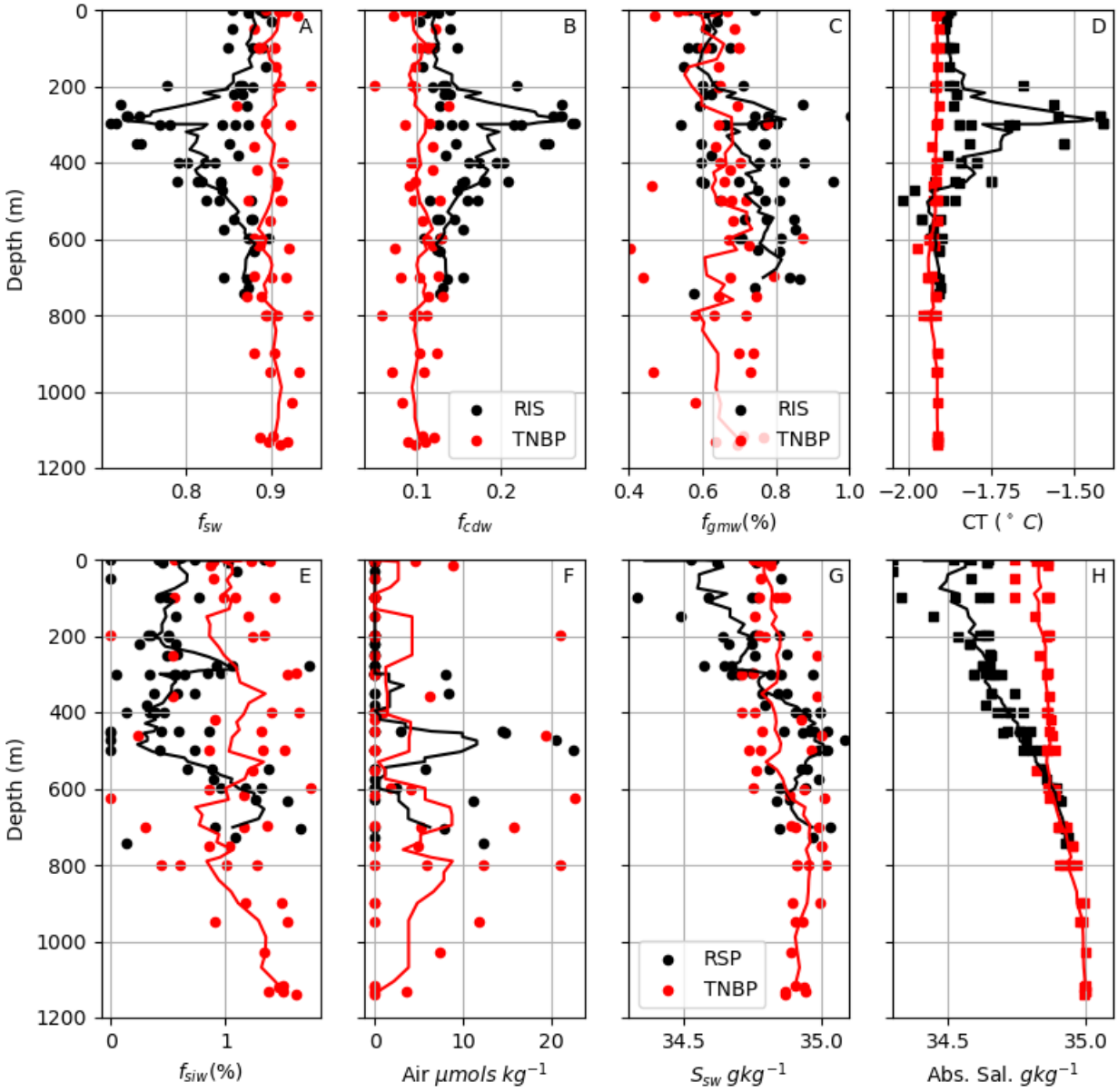

Figure 4: Scatter plots of the NGPT model result in panels A-C and E-G within the Terra Nova Bay and Ross Ice Shelf Polynyas. The solid lines indicate a 10-point vertical running average of the scatter points.

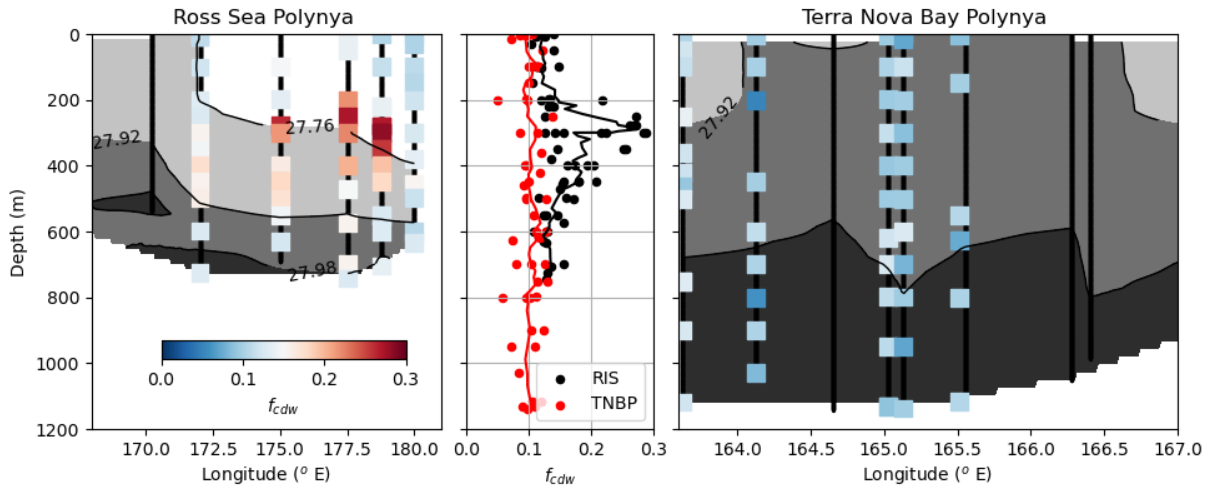

Figure 5: A spatial breakout of the CDW distribution in the Ross Sea and Terra Nova Bay polynyas. The gray shading and black contour lines are the potential density anomaly ($\boldsymbol{\sigma_\theta}$), computed using absolute salinity and conservative temperature.

2.1 S_{sw} and In-situ salinity

The in-situ salinity and NGPT model output salinity (S_{sw}) are largely in agreement in both polynyas. In-situ salinity is nearly isohaline above 600 m in TNBP. In contrast, there is monotonic salinity decrease, reflecting persistent stratification in the Ross Ice Shelf Polynya. These same patterns are more or less reflected in S_{sw}, although S_{sw} is slightly greater than in-situ salinity in the RSP and overall slightly less than in-situ salinity in the TNBP.

2.2 Glacial meltwater distributions:

GMW in the RSP is broadly sourced from the melting of the Ross Ice Shelf, and associated with CDW intrusions. The intrusion of CDW near 300 m in the RSP (Fig. 4) is also associated with one of two extrusions of glacial meltwater (Fig. 6). The most prominent appears at 300 m, coinciding with the temperature maximum. This feature of elevated meltwater is found near the dateline at 180° and is known as the furthest west extrusion of glacial meltwater from under the ice shelf (Loose et al., 2009; Smethie & Jacobs, 2005). The extrusion of GMW between 500 and 600 m may be associated with DSW and the production of ice shelf water with temperatures below -2 °C (Smethie and Jacobs 2005; Loose et al. 2009). In addition to the local production of GMW, the

RSP profiles likely also reflect meltwater import from upstream in the Amundsen and Bellingshausen seas, especially near the surface with transport via the Antarctic Coastal Current.

The meltwater distribution in TNBP is relatively more uniform with lower content than what is found in the RSP; the mean meltwater content in the RSP is 0.7% versus 0.6% in the TNBP. The meltwater content found in TNBP is likely associated with melting at the base and edges of the Drygalski Ice Tongue as well as from the Hells Gate and Nansen ice shelves (Frezzotti 1993).

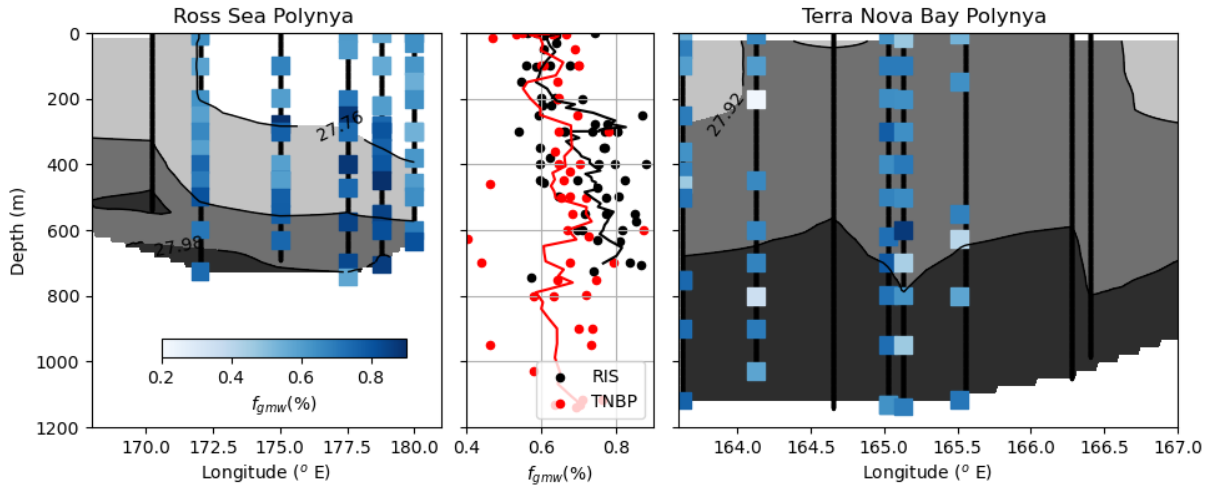

Figure 6: A spatial breakout of the glacial meltwater (GMW) distribution in the Ross Sea and Terra Nova Bay polynyas. The highest meltwater concentrations in the RSP coincide with the highest quantity of CDW, near 300 m. The gray shading and black contour lines are the potential density anomaly (σ_θ), computed using absolute salinity and conservative temperature.

2.3 Sea ice water distributions

The vertical distribution of sea ice water reveals the differences in seasonal evolution between the RSP and TNBP in 2017. As we reported in Section 0.1, the mixed-layer depth was significantly shallower in the Ross Sea - reaching an average depth of 250 m, compared to 650 m in the central part of the Terra Nova Bay polynya. In this circumstance, we will interpret the SIW fractions separately from within and below the mixed-layer, because they effectively represent two different years. The SIW fractions beneath the mixed layer are a remnant of the integrated sea ice melt from the 2016 freeze season, provided the polynya mixes to the bottom during winter.

By the same mechanism, the mixed-layer SIW fractions represent ice formation from the 2017 freeze season. In the upper 250 m of the RSP, the average SIW fraction was 0.5%; between 250 m and the bottom of the RSP profiles at 800 m, the average SIW fraction was 0.7%. In comparison, the average fraction of SIW within the mixed-layer of TNB was 1.04%. Below 650 m, this value increased to an average of 1.15%. That is, the SIW percentages were more than 50% greater in TNBP mixed-layer in 2017, compared to the RSP mixed-layer. This coincides with a big difference in wind speed for these two regions: In 2017, the automated weather station data (AWS) from the edge of the Ross Ice Shelf (Station Vito) showed a mean wind speed of 5.7 m s^{-1} between April and October. During the same period, the mean wind speed at the nearest AWS to Terra Nova Bay was 20.3 m s^{-1}.

In the Ross Ice Shelf Polynya during 2017/2016, ice production reached 1.35/5.52 meters of ice and in Terra Nova Bay polynya, ice production was 6.76/14.95 meters of ice. To obtain the 2017 estimates we multiplied the depth of the mixing column in 2017 by the fraction of SIW; to obtain the ice production in 2016, we multiplied the mean value of SIW found below the mixing column by the full depth of the water column - 800 m and 1300 m for the RSP and TNBP respectively. This invokes the assumption that the values below the mixed-layer are a record of the *entire* water column SIW fractions during the previous winter, when the polynyas last mixed to the bottom. For comparison purposes, these annual ice production estimates can be converted to average daily ice production rates for the season of freezing. Remote sensing estimates of ice production use the period from March to October or 214 days to capture the freezing period (Ohshima et al. 2016), so we have divided the total ice production by this duration in the 2016 calculations. For the 2017 calculations, PIPERS measurements occurred in the TNBP between May 1 and 11 or approximately 72 days into the freeze season, and between May 16 and 21 in the RSP; 82 days into the freeze season. This suggests an ice production rate of 1.5 cm d^{-1} for the RSP and 9.3 cm d^{-1} in the TNBP by mid-May in 2017 (Table 2). If the same rate of ice production persisted throughout the freezing season, it would be equivalent to 3.3 m of ice production in the RSP and 20.1 m ice production in the TNBP during 2017.

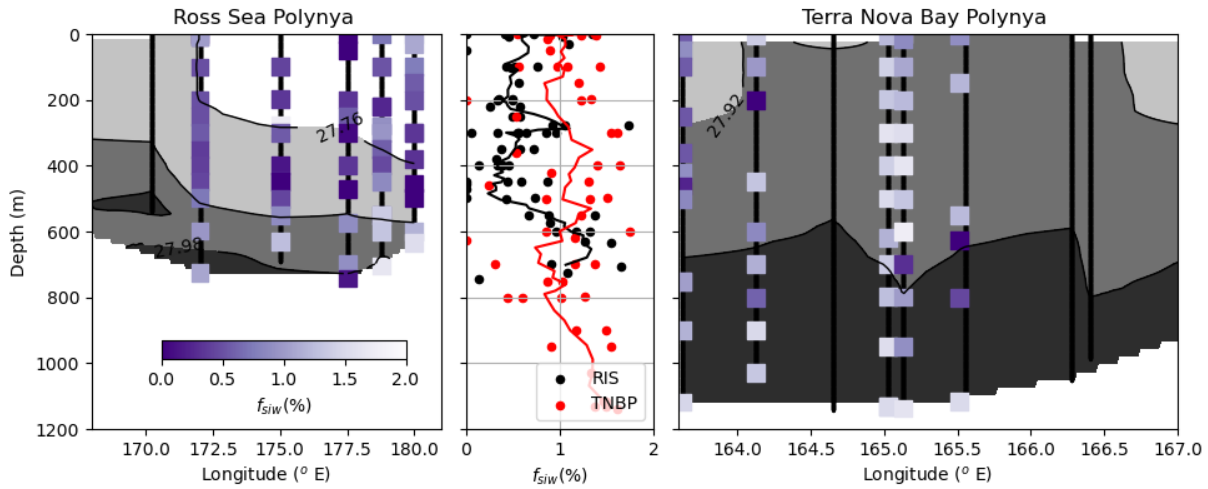

Figure 7: A spatial breakout of the percentage of seawater removed as sea ice or 'sea ice water' (SIW) within the Ross Sea and Terra Nova Bay polynyas. The profiles reveal highest SIW concentrations in the deepest portion of the TNBP mixed layer, near 165 °E. The gray shading and black contour lines are the potential density anomaly ($\boldsymbol{\sigma_\theta}$), computed using absolute salinity and conservative temperature.

These values suggest that the seasonal ice production rate per unit area is 2.6 times greater in TNBP in 2016 and 6 times greater in 2017 than in the RSP (while noting that the water column values of SIW in 2017 only capture the first one third of the 2017 freezing season). Petrelli et al. (2008) report a production rate in TNBP that is 1.6 times that of the RSP. In 2017, the wind speeds in TNBP were 3.5 times higher than in the RSP; when considering that heat loss is proportional to the square of the wind speed, it is perhaps not unreasonable to expect so much more sea ice production in Terra Nova Bay under these conditions in 2017.

Table 2: Estimates of the annual ice production in meters, and the seasonal average ice production in cm d^{-1}, for the RSP and TNBP using the mixed-layer depths and the vertical average of SIW within the mixed-layer for 2017 and beneath the mixed-layer for 2016. In addition, Table 2 lists the prior ice production estimates and their associated estimation methods.

This study	f_{siw} (%)	Column depth (m)	Seasonal average (cm/d)	Annual ice production (m)
RSP, 2016	0.7	800	2.6	5.6
RSP, 2017	0.5	250	1.5	3.3
TNBP, 2016	1.15	1300	7.0	15
TNBP, 2017	1.04	650	9.3	20.1
Previous study	**Estimate type**		**Seasonal average (cm/d)**	**Annual ice production (m)**
TNBP, Shick (2018)	Heat budget		–	27
TNBP, Petrelli et al., (2008)	Ocean model		7.7-11.0	–
RSP, Petrelli et al., (2008)	Ocean model		7.0	–
TNBP, Ohshima et al., (2016)	AMSR-E radiometer, thin ice algorithm		3.9	–
RSP, Ohshima et al., (2016)	AMSR-E radiometer, thin ice algorithm		3.5	–
TNBP, Nakata, (2021)	AMSR-E radiometer, thin ice algorithm with frazil ice		–	> 20

These values fall within the range of previous estimates of annual ice growth in TNBP, although the estimates from the Ross Ice Shelf Polynya are lower than most previous estimates in the literature. An analysis of ice production by Schick (2018) estimated the spatial gradient in air-sea heat fluxes along an upstream-downstream axis in the TNBP using a series of UAS flights collected in 2009 and 2012. These spatial gradients were merged with 7 years of Automated Weather Station (AWS) data to develop a winter climatology of heat flux and ice production. Overall, these estimates reveal 3-5 m of ice production per month between April and October or

454 an average of 27 m in annual ice production, which is 20 to 45 % higher than our 2016 and 2017
455 estimates. Petrelli et al. (2008) simulated a strong and a weak winter in TNB and a strong winter
456 in RSP. The strong and weak winters in TNB produced seasonal averages of 7.7 up to 11.0 cm d^{-1}
457 , which are in accord with our estimates for 2016 and 2017 in TNBP. In the RSP, a winter of
458 intense ice formation yielded 7.0 cm d^{-1}, which is 70-100% greater than what these water column
459 estimates produced with 5.6 and 3.8 cm d^{-1}. Previous remote sensing algorithms have shown the
460 greatest discrepancies, when comparing with in-situ heat budget and our water column
461 estimates. For example, Ohshima et al. (2016) produced mean estimates over 9 winters to yield
462 3.5 cm d^{-1} for the RSP and 3.9 cm d^{-1} for the TNBP using the thin ice algorithm for AMSR-E
463 developed by Nihashi and Ohshima (2015). However, these algorithms have been modified to
464 detect frazil ice formation and this change has significantly increased the estimates of annual ice
465 production to greater than 20 m/yr, including in Terra Nova Bay (Nakata et al. 2021). Last, we
466 note that two PIPERS-related studies of Terra Nova Bay polynya have invoked the potential for
467 sea spray to enhance heat loss (Guest 2021) and sea ice production, perhaps by as much as 40%
468 , at least within the open water areas of the polynya. While there were no direct measurements
469 of sea spray during PIPERS, wave buoy estimates of mean square slope suggest some waves were
470 steep enough to experience breaking and production of sea spray (Ackley et al. 2022). It remains
471 difficult to determine what portion of the polynya is open water and what portion is frazil ice-
472 covered water, during katabatic wind events; results from Nakata et al., (2021) and the rapid
473 decrease in atmospheric heat flux, suggest some open water may extend as far as 25-30 km from
474 the coast in both the RSP and TNBP, which is a relatively narrow region compared to the overall
475 polynya area.

476 These estimates represent some of the first estimates of ice production using water
477 column measurements of dissolved gas tracers. The results fall within the range of prior
478 production estimates for these same polynyas, and reveal another method for estimating the
479 integrated ice production over the course of a season or over the time period since the water
480 column last mixed. For our purposes, the agreement in ice seasonal production rates with other
481 estimates adds circumstantial validation to the NGPT estimates of water column SIW fractions,
482 supporting the further interpretation of the SIW fractions.

2.4 Air bubble injection

The air content in both polynyas was lower than expected: the average air content injected was 2.7 umol kg^{-1} in TNBP and 1.1 umol kg^{-1} in RSP, although there is a high degree of variation in the individual estimates from the NGPT model: Most of the values are zero or negligible, but a subset of points in both polynyas yielded individual estimates approaching 25 umol kg^{-1}. In the Ross Ice Shelf Polynya, these values are found below 400 m, perhaps reflecting the low winds and lack of surface turbulence in the RSP in 2017. In TNBP the air injection is also weighted toward deeper depths, but also exhibits some elevated air injection further up in the water column.

There have been several model and data-based evaluations of air bubble injection in the ocean. Several previous studies have computed bubble injection fluxes that translate to between 1.2 and 2.5% excess Argon on average between 1000 and 5000 m (Stanley et al. 2009; Nicholson et al. 2011; Liang et al. 2013). Because air injection results in quantitative dissolution of gases at the mixing ratios for the atmosphere, these argon excesses translate to between 26 and 44 umol kg^{-1} of excess air from bubble injection. Therefore, the air bubble content in the Ross Ice Shelf Polynyas is between 2.5 and 10% of the global estimates.

These low values of air injection seem even less congruous when we consider the influence of katabatic winds ranging from 16 to 27 m s^{-1} during the period of PIPERS field data collection in Terra Nova Bay. One LES model study of air bubble injection reveals that winds above 20 m s^{-1} resulted in excess argon saturation up to 6% (Fig. 3, Liang et al., 2013) or 105 umol kg^{-1} suggesting the estimated values of air bubble injection might be as small as 1% of the expected open ocean value for these forcing conditions.

The explanation for such a strong limitation in air bubble injection is most likely tied to frazil ice production and accumulation of crystals in the surface layer. Frazil ice, or disaggregated ice crystals in seawater can reach concentrations where the interactions between fluids and the suspended particles changes the rheology of the flow (Ayel et al. 2003; Matsumura and Ohshima 2015). These types of fluids are referred to as two-phase flows, analogous to slurries composed of sediment and water. Such were the conditions we found, particularly in the TNBP, which was extensively covered by frazil ice. Model studies of Matsumura and Ohshima (2015) reveal that

512 frazil ice concentrations of up to 100 g of ice per m^3 can exist to depths of 30 m or greater in the
513 surface ocean. These results match the observations of Thompson et al. (2020) who observed
514 heat and salt anomalies between 10 and 50 m below the water surface during the PIPERS
515 expedition. As turbulence is attenuated, the crystals will migrate buoyantly to the surface to
516 become incorporated into a consolidated ice pack. The visible imagery recorded in Terra Nova
517 Bay during PIPERS shows that at the surface, the frazil ice is organized into wind rows, likely a
518 consequence of Langmuir cells (Ackley et al. 2020; Thompson et al. 2020). This can be explained
519 in part by the increase in viscosity: using the ice-dependent viscosity equation from Matsumura
520 and Ohshima (2015), water viscosity increases by nearly 40% for every 10% increase in frazil ice
521 fraction (see Figure S2). These changes in viscosity also imply a decrease in the diffusive gas
522 transfer velocity - with a reduction in gas transfer velocity (k) of 20% for every 10% increase in
523 frazil ice; thus comparatively less gas will enter the water by turbulent diffusion. As the frazil
524 crystals migrate buoyantly toward the surface ocean, they produce a surface layer that is elastic
525 with respect to ocean waves, but with a significant increase in surface tension that limits breaking
526 and bubble entrainment. Lab and field studies by Martin and Kauffmann (1981) illustrate rapid
527 decays in surface gravity wave amplitude, and the same phenomenon influences wave breaking
528 as wave steepness is quickly attenuated (Ackley et al. 2022). In this environment, all types of air-
529 sea gas exchange are suppressed; air bubble injection appears to be strongly limited because of
530 its dependence on breakage of the water surface.
531 While we assert that there are several lines of physical evidence to support a suppression
532 in air bubble injection, it is worth recalling that we noted two other PIPERS studies in Section
533 2.3m that suggest sea spray production by wave tearing may have been important to air-sea heat
534 flux (Guest 2021) and ice production. These are the sort of conditions often associated with air
535 bubble injection, which appears to contradict our results. While there were no direct
536 measurements of sea spray during PIPERS, wave buoy estimates of mean square slope suggest
537 some waves were steep enough to experience breaking and production of sea spray (Ackley et
538 al. 2022). The net effect of open water bubble injection depends on the polynya surface area that
539 free of frazil and consolidated ice. It remains difficult to determine what portion of the polynya
540 is open water and what portion is frazil ice-covered water, during katabatic wind events; results

from Nakata et al., (2021) and the rapid decrease in atmospheric heat flux, suggest some open water may extend as far as 25-30 km from the coast in both the RSP and TNBP, which is a relatively narrow region compared to the overall polynya area.

3.0 The physical processes setting deep water solubility conditions

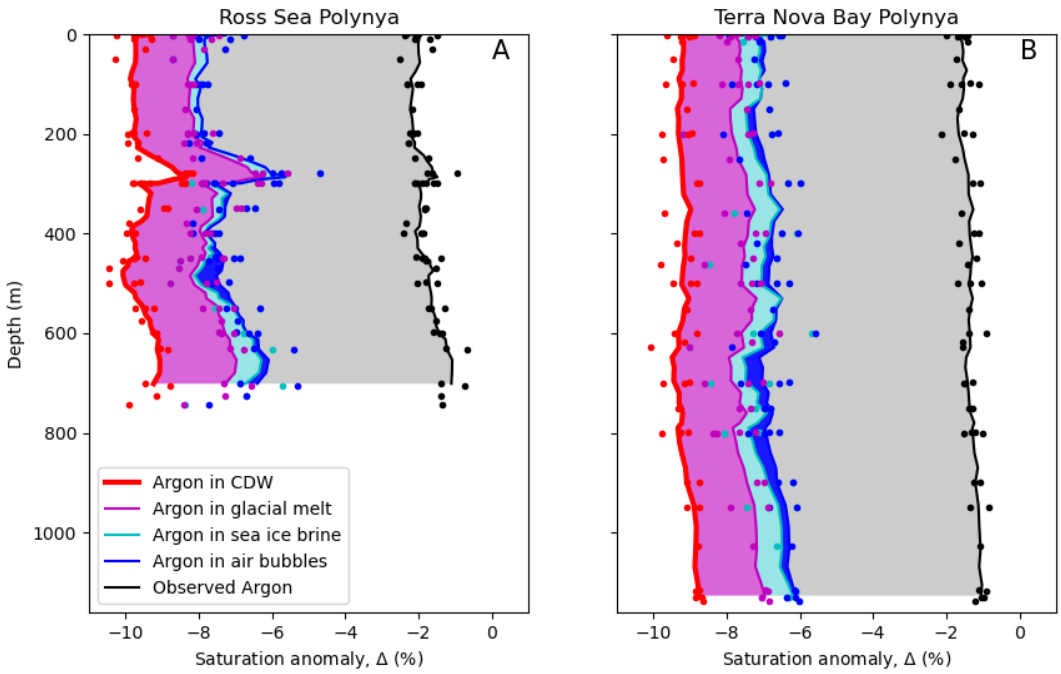

Figure 8: The contribution of ice processes to the ventilation of Circumpolar Deep Water, as it is transformed into Dense Shelf Water: The areas shaded by color represent the contribution of each process to the restoration of argon saturation within DSW, including glacial melt (magenta), sea ice brine (light blue), and air injection (dark blue). The gray shaded area represents the remaining deficit, which we attribute to diffusive air-sea gas exchange. Panel A depicts the water column in the Ross Ice Shelf Polynya, Panel B reveals the same in the Terra Nova Bay Polynya.

Referring back to the schematic model described in (Figure 3), the water in the Ross Sea is primarily composed of modified-CDW that crosses the continental shelf break and is modified via surface and ice processes. This modified water mass receives inputs primarily from glacial and sea ice melt, although precipitation as snow may make a contribution in some coastal seas.

558 During the modification process, CDW cools and freshens, especially as it becomes modified
559 during winter heat loss in polynyas, the temperature decreases to below the freezing point or -
560 1.95 ℃ as observed in the mixed-layer, during the PIPERS expedition. This cooling increases the
561 capacity of this water to absorb gas, and that is reflected in the saturation anomalies depicted in
562 Figure 2.

563 To illustrate the role of the freshwater inputs and air-sea processes on the solubility pump
564 on shelf water we recompose the budget of dissolved argon in the Ross and Terra Nova Bay
565 polynyas (Figure 8), using the saturation anomaly, where in-situ conservative temperature and
566 absolute salinity dictate the equilibrium solubility for argon in the water column. By convention,
567 we have assumed 1 atmosphere of pressure in computing these argon saturation anomalies, as
568 well as the anomalies found in Figure 2. As noted in Section 1.0, the NGPT model assumes an
569 ambient sea level pressure of 0.97 atm, but we do not adopt that value in presenting the
570 saturation anomalies, so that they can be more globally comparable.

571 Old circumpolar water that is modified in the Ross Sea, begins with a dissolved argon
572 content of 16.3 umol/kg, which represents a saturation anomaly of -6% compared to shelf
573 waters. This value is taken as the average of argon in the core of CDW near 500 m offshore in the
574 Weddell Sea (Loose et al. 2016), because we lack measurements of argon offshore of the Ross
575 Sea. Ice processes - glacial meltwater intrusion and sea ice formation- are both sources of
576 dissolved argon to the water column: Gmw restores 1.8% of the argon saturation anomaly in the
577 RSP and 1.6% in TNB polyna, and SIW restores an additional 0.33% and 0.5% of the 6% deficit to
578 each polynya respectively. Even though sea ice formation removes both water and gas from the
579 polynya water column, this addition of gases is associated with brine rejection so that the net
580 effect on water column concentrations is to enhance the dissolved gases (and salt).

581 Comparatively, air bubble injection leads to the smallest total restoration of gas to the
582 water column. In the Ross Ice Shelf Polynya, air bubble injection restored 0.11% to the argon
583 saturation anomaly and in the comparatively-windier Terra Nova Bay polynya that restoration
584 was 0.18%. Summing it all up, we observe that cryogenic processes restore 27.5% of the argon
585 deficit in dense shelf water; air bubble injection accounts for an additional 1.4%, and we infer

586 that the remainder (71%, gray shaded area in Fig. 8) is restored by mixing and air-sea gas
587 exchange.
588
589 **4.0 Summary**
590 These results reveal how physical processes stack up to restore the gas solubility deficit
591 in dense shelf water, as it forms during the extreme conditions that take place in latent heat
592 polynyas during winter. Previous studies evaluating the impact of ice on the solubility pump have
593 focused solely on how the sea ice cover acts to restrict the rate of air-sea gas exchange (Keeling
594 1993; Toggweiler et al. 2003; Nicholson et al. 2010; Sigman et al. 2010). In particular, Toggweiler
595 et al., (2003) demonstrated how the reduction of the surface area of the southern outcrop of the
596 MOC leads to an increase in the air-sea pCO_2 differential and therefore a decrease in the solubility
597 pump. This work reveals that the sole focus on inhibition of air-sea gas exchange overlooks the
598 additional ice-associated processes that also influence the restoration of gases in actively forming
599 dense shelf water, including sea-ice formation and glacial meltwater inputs. As we consider the
600 implications of these results from the NGPT model, they suggest that the transport of impurities
601 during ice freeze and melt is of increasing significance while perhaps the particular mechanisms
602 of gas exchange, such as bubble injection are less impactful. Therefore we need more detailed
603 knowledge of how impurities in seawater behave when confronted with the freezing process. In
604 this study, we have used the equilibrium partition coefficients for the noble gases to
605 parameterize how gas is separated between ice and water, which have been developed for more
606 mature ice conditions. But in the polynya, it is becoming apparent that frazil ice is the ice type
607 that may be most associated with DSW formation (Tison et al. 2020; Thompson et al. 2020;
608 Nakata et al. 2021) (Tison, Nakata, Thompson). It is likely that as individual frazil ice crystals
609 nucleate, the separation of gases is even more efficient than for mature columnar ice, favoring
610 the deposition of impurities in the water column, but behavior of dissolved ions and gases under
611 these conditions is unknown.
612 Finally, this work can be extended to consider the influence of ice processes on the
613 restoration of important biogenic gases like oxygen and carbon dioxide in DSW, however that

614 also requires the ability to distinguish between the biological and physical contributions, which
615 we will leave to a forthcoming study.
616
617
618
619 **Acknowledgements**
620
621 This work was supported by the National Science Foundation Awards ANT-1341630 (B. Loose),
622 ANT-1341717 (S.F.Ackley), ANT-1341606 (S. Stammerjohn), ANT-1543483 (P. Sedwick). The
623 authors would like to thank the staff of the Antarctic Support Contractor for their efforts to gather
624 high quality data in the challenging environment of the Ross Sea in late Fall.
625
626 **Data Availability**
627
628 The noble gas data is available at the US Antarctic Program Data Center (https://www.usap-
629 dc.org/search). Hydrographic data is available through the Marine Geoscience Data System
630 (https://www.marine-geo.org/tools/search/entry.php?id=NBP1704).
631
632
633
634
635
636
637
638
639
640
641
642

643
644
645
646
647
648 **References:**
649
650 Ackley, S. F., M. Smith, P. S. Gueste, A. Herman, and H. Shen. 2022. Winds, Waves and Ice
651 Formation in a Coastal Polynya. Proceedings of the 26th IAHR International Symposium
652 on Ice.
653 Ackley, S. F., S. Stammerjohn, T. Maksym, and others. 2020. Sea-ice production and
654 air/ice/ocean/biogeochemistry interactions in the Ross Sea during the PIPERS 2017
655 autumn field campaign. Ann. Glaciol. **61**: 181–195. doi:10.1017/aog.2020.31
656 Aeschbach-Hertig, W., and D. K. Solomon. 2013. Noble Gas Thermometry in Groundwater
657 Hydrology, p. 81–122. *In* P. Burnard [ed.], The Noble Gases as Geochemical Tracers.
658 Springer Berlin Heidelberg.
659 Allan, R., and T. Ansell. 2006. A New Globally Complete Monthly Historical Gridded Mean Sea
660 Level Pressure Dataset (HadSLP2): 1850–2004. J. Clim. **19**: 5816–5842.
661 doi:10.1175/JCLI3937.1
662 Ayel, V., O. Lottin, and H. Peerhossaini. 2003. Rheology, flow behaviour and heat transfer of ice
663 slurries: a review of the state of the art. Int. J. Refrig. **26**: 95–107. doi:10.1016/S0140-
664 7007(02)00016-6
665 Broecker, W., J. Lynch-Stieglitz, D. Archer, M. Hofmann, E. Maier-Reimer, O. Marchal, T.
666 Stocker, and N. Gruber. 1999. How strong is the Harvardton-Bear constraint? Glob.
667 Biogeochem. Cycles **13**: 817–820.
668 Cheon, W. G., S.-K. Lee, A. L. Gordon, Y. Liu, C.-B. Cho, and J. J. Park. 2015. Replicating the

669 1970s' Weddell Polynya using a coupled ocean-sea ice model with reanalysis surface
670 flux fields. Geophys. Res. Lett. **42**: 5411–5418. doi:10.1002/2015GL064364
671 Cliff, E., S. Khatiwala, and A. Schmittner. 2021. Glacial deep ocean deoxygenation driven by
672 biologically mediated air–sea disequilibrium. Nat. Geosci. **14**: 43–50.
673 doi:10.1038/s41561-020-00667-z
674 Costanza, C. A., M. A. Lazzara, L. M. Keller, and J. J. Cassano. 2016. The surface climatology
675 of the Ross Ice Shelf Antarctica. Int. J. Climatol. **36**: 4929–4941. doi:10.1002/joc.4681
676 Feltham, D. L., N. Untersteiner, and J. S. Wettlaufer. 2006. Sea ice is a mushy layer. Geophys.
677 Res. Lett. **33**. doi:10.1029/2006GL026290
678 Frezzotti, M. 1993. Glaciological study in Terra Nova Bay, Antarctica, inferred from remote
679 sensing analysis. Ann. Glaciol. **17**: 63–71. doi:10.3189/S0260305500012623
680 Gade, H. 1979. Melting of ice in sea water: A primitive model with application to the Antarctic ice
681 shelf and icebergs. J. Phys. Oceanogr. **9**: 189–198.
682 Garandet, J., J. Favier, and D. Camel. 1994. Segregation phenomena in crystal growth from the
683 melt. Handb. Cryst. Growth **2**: 659–705.
684 Gordon, A. L., B. Huber, D. McKee, and M. Visbeck. 2010. A seasonal cycle in the export of
685 bottom water from the Weddell Sea. Nat. Geosci. **3**: 551–556. doi:10.1038/ngeo916
686 Guest, P. S. 2021. Inside Katabatic Winds Over the Terra Nova Bay Polynya: 2. Dynamic and
687 Thermodynamic Analyses. J. Geophys. Res. Atmospheres **126**: e2021JD034904.
688 doi:10.1029/2021JD034904
689 Hamme, R. C., D. P. Nicholson, W. J. Jenkins, and S. R. Emerson. 2019. Using Noble Gases to
690 Assess the Ocean's Carbon Pumps. Annu. Rev. Mar. Sci. **11**: 75–103.
691 doi:10.1146/annurev-marine-121916-063604
692 Hamme, R. C., and J. P. Severinghaus. 2007. Trace gas disequilibria during deep-water
693 formation. Deep-Sea Res. Part I **54**: 939–950.
694 Hood, E. M., B. L. Howes, and W. J. Jenkins. 1998. Dissolved gas dynamics in perennially ice-

covered Lake Fryxell, Antarctica. Deep Sea Res. **50**: 265–272.

Jacobs, S. S., and C. F. Giulivi. 2010. Large Multidecadal Salinity Trends near the Pacific–Antarctic Continental Margin. J. Clim. **23**: 4508–4524. doi:10.1175/2010JCLI3284.1

Jacobs, S. S., C. F. Giulivi, and P. Dutrieux. 2022. Persistent Ross Sea Freshening From Imbalance West Antarctic Ice Shelf Melting. J. Geophys. Res. Oceans **127**: e2021JC017808. doi:10.1029/2021JC017808

Jacobs, S. S., C. F. Giulivi, and P. A. Mele. 2002. Freshening of the Ross Sea During the Late 20th Century. Science **297**: 386–389. doi:10.1126/science.1069574

Jenkins, A. 1999. The Impact of Melting Ice on Ocean Waters. J. Phys. Oceanogr. **29**: 2370–2381. doi:10.1175/1520-0485(1999)029<2370:tiomio>2.0.co;2

Jenkins, W. J. 2020. Using Excess 3He to Estimate Southern Ocean Upwelling Time Scales. Geophys. Res. Lett. **47**: e2020GL087266. doi:10.1029/2020GL087266

Keeling, R. F. 1993. On the role of large bubbles in air-sea gas exchange and supersaturation in the ocean. J. Mar. Res. **51**: 237–271.

Killawee, J. A., I. J. Fairchild, J.-L. Tison, L. Janssens, and R. Lorrain. 1998. Segregation of solutes and gases in experimental freezing of dilute solutions: Implications for natural glacial systems. Geochim. Cosmochim. Acta **62**: 3637–3655.

de Lavergne, C., J. B. Palter, E. D. Galbraith, R. Bernardello, and I. Marinov. 2014. Cessation of deep convection in the open Southern Ocean under anthropogenic climate change. Nat. Clim Change **4**: 278–282.

Liang, J.-H., C. Deutsch, J. C. McWilliams, B. Baschek, P. P. Sullivan, and D. Chiba. 2013. Parameterizing bubble-mediated air-sea gas exchange and its effect on ocean ventilation. Glob. Biogeochem. Cycles **27**: 894–905. doi:10.1002/gbc.20080

Loose, B., and W. J. Jenkins. 2014. The five stable noble gases are sensitive unambiguous tracers of glacial meltwater: LOOSE AND JENKINS; NOBLE GASES ARE TRACERS OF MELTWATER. Geophys. Res. Lett. **41**: 2835–2841. doi:10.1002/2013GL058804

721 Loose, B., W. J. Jenkins, R. Moriarty, and others. 2016. Estimating the recharge properties of
722 the deep ocean using noble gases and helium isotopes. J. Geophys. Res. Oceans.
723 doi:10.1002/2016JC011809
724 Loose, B., P. Schlosser, W. M. Smethie, and S. Jacobs. 2009. An optimized estimate of glacial
725 melt from the Ross Ice Shelf using noble gases, stable isotopes, and CFC transient
726 tracers. J. Geophys. Res. **114**. doi:10.1029/2008JC005048
727 Martin, S., and P. Kauffman. 1981. A field and laboratory study of wave damping by grease ice.
728 J. Glaciol. **27**: 283–313.
729 Martinierie, P., D. Raynaud, D. M. Etheridge, J.-M. Barnol, and D. Mazaudier. 1992. Physical
730 and climatic parameters which influence the air content in polar ice. Earth Planet. Sci.
731 Lett. **112**: 1–13.
732 Matsumura, Y., and K. I. Ohshima. 2015. Lagrangian modelling of frazil ice in the ocean. Ann.
733 Glaciol. **56**: 373–382.
734 Morrison A. K., Hogg A. McC., England M. H., and Spence P. 2020. Warm Circumpolar Deep
735 Water transport toward Antarctica driven by local dense water export in canyons. Sci.
736 Adv. **6**: eaav2516. doi:10.1126/sciadv.aav2516
737 Nakata, K., K. I. Ohshima, and S. Nihashi. 2021. Mapping of Active Frazil for Antarctic Coastal
738 Polynyas, With an Estimation of Sea-Ice Production. Geophys. Res. Lett. **48**:
739 e2020GL091353. doi:10.1029/2020GL091353
740 Namiot, A. Y., and E. B. Bukhgalter. 1965. Clathrates formed by gases in ice. J. Struct. Chem.
741 **6**: 873–874.
742 Nicholson, D., S. Emerson, N. Caillon, J. Jouzel, and R. C. Hamme. 2010. Constraining
743 ventilation during deepwater formation using deep ocean measurements of the dissolved
744 gas ratios 40Ar/36Ar, N2/Ar, and Kr/Ar. J Geophys Res **115**: C11015.
745 doi:10.1029/2010jc006152
746 Nicholson, D. P., S. R. Emerson, S. Khatiwala, and R. C. Hamme. 2011. An inverse approach to

747 estimate bubble-mediated air-sea gas flux from inert gas measurements. Proceedings of
748 the Proceedings on the 6th International Symposium on Gas Transfer at Water
749 Surfaces. Kyoto Univ. Press Kyoto, Japan. 223–237.
750 Nihashi, S., and K. I. Ohshima. 2015. Circumpolar Mapping of Antarctic Coastal Polynyas and
751 Landfast Sea Ice: Relationship and Variability. J. Clim. **28**: 3650–3670.
752 doi:10.1175/JCLI-D-14-00369.1
753 Ohshima, K. I., Y. Fukamachi, G. D. Williams, and others. 2013. Antarctic Bottom Water
754 production by intense sea-ice formation in the Cape Darnley polynya. Nat. Geosci **6**:
755 235–240. doi:10.1038/ngeo1738
756 Ohshima, K. I., S. Nihashi, and K. Iwamoto. 2016. Global view of sea-ice production in polynyas
757 and its linkage to dense/bottom water formation. Geosci. Lett. **3**: 13.
758 doi:10.1186/s40562-016-0045-4
759 Orsi, A. H., and C. L. Wiederwohl. 2009. A recount of Ross Sea waters. Deep-Sea Res. II.
760 doi:10.1016/ j.dsr2.2008.10.033
761 Padman, L., S. L. Howard, A. H. Orsi, and R. D. Muench. 2009. Tides of the northwestern Ross
762 Sea and their impact on dense outflows of Antarctic Bottom Water. South. Ocean Shelf
763 Slope Exch. **56**: 818–834. doi:10.1016/j.dsr2.2008.10.026
764 Petrelli, P., N. Bindoff, and A. Bergamasco. 2008. The sea ice dynamics of Terra Nova Bay and
765 Ross Ice Shelf Polynyas during a spring and winter simulation. J. Geophys. Res.
766 Oceans **113**.
767 Schick, K. E. : 2018. Influences of Weather and Surface Variability on Sensible Heat Fluxes in
768 Terra Nova Bay, Antarctica. University of Colorado.
769 Sigman, D. M., M. P. Hain, and G. H. Haug. 2010. The polar ocean and glacial cycles in
770 atmospheric CO2 concentration. Nature **466**: 47–55. doi:10.1038/nature09149
771 Silvano, A., S. Rintoul, B. Peña-Molino, W. R. Hobbs, van W. Esmee, Aoki Shigeru, Tamura
772 Takeshi, and Williams Guy Darvall. 2018. Freshening by glacial meltwater enhances

melting of ice shelves and reduces formation of Antarctic Bottom Water. Sci. Adv. **4**: eaap9467. doi:10.1126/sciadv.aap9467

Smethie, W. M., and S. S. Jacobs. 2005. Circulation and melting under the Ross Ice Shelf: estimates from evolving CFC, salinity and temperature fields in the Ross Sea. Deep-Sea Res. **52**: 959–978.

Stanley, R. H. R., W. J. Jenkins, D. E. I. Lott, and S. C. Doney. 2009. Noble gas constraints on air-sea gas exchange and bubble fluxes. J Geophys Res **114**. doi:10.1029/2009JC005396

Stute, M., and P. Schlosser. 1993. Principles and Applications of the Noble Gas Paleothermometer, p. 89–100. *In* Climate Change in Continental Isotopic Records. American Geophysical Union.

Tamura, T., K. Ohshima, and S. Nihashi. 2008. Mapping of sea ice production for Antarctic coastal polynyas. Geophys. Res. Lett. **35**. doi:10.1029/2007GL032903

Thomas, D. N., and G. S. Dieckmann. 2010. Sea ice, 2nd ed. Wiley-Blackwell.

Thompson, L., M. Smith, J. Thomson, S. Stammerjohn, S. Ackley, and B. Loose. 2020. Frazil ice growth and production during katabatic wind events in the Ross Sea, Antarctica. The Cryosphere **14**: 3329–3347. doi:10.5194/tc-14-3329-2020

Tison, J.-L., T. Maksym, A. D. Fraser, and others. 2020. Physical and biological properties of early winter Antarctic sea ice in the Ross Sea. Ann. Glaciol. **61**: 241–259.

Toggweiler, J. R., A. Gnanadesikan, S. Carson, R. Murnane, and J. L. Sarmiento. 2003. Representation of the carbon cycle in box models and GCMs: 1. Solubility pump. Glob. Biogeochem. Cycles **17**. doi:10.1029/2001GB001401

Tomczak, M. 1981. A multiparameter extension of temperature/salinity diagram techniques for the analysis of non-isopycnal mixing. Prog. Oceanogr. **10**: 147–171.

Tomczak, M., and D. G. B. Large. 1989. Optimum multiparameter analysis of mixing in the thermocline of the eastern Indian Ocean. J. Geophys. Res. Oceans **94**: 16141–16149.

799 doi:10.1029/JC094iC11p16141
800 Top, Z., S. Martin, and P. Becker. 1988. A laboratory study of dissolved noble gas anomaly due
801 to ice formation. Geophys. Res. Lett. **15**: 796–799. doi:10.1029/GL015i008p00796
802 Wettlaufer, J. S. 1992. Directional solidification of salt water: Deep and shallow cells. Europhys.
803 Lett. **19**: 337–342.
804 Williams, G., L. Herraiz-Borreguero, F. Roquet, and others. 2016. The suppression of Antarctic
805 bottom water formation by melting ice shelves in Prydz Bay. Nat. Commun. **7**: 1–9.
806
807
808